THE STRUCTURE OF TURBULENCE IN A SHALLOW WATER WIND-DRIVEN SHEAR CURRENT WITH LANGMUIR CIRCULATION

Andrés E. Tejada-Martínez and Chester E. Grosch
Center for Coastal Physical Oceanography, Old Dominion University
Norfolk, Virginia 23529, USA
tejada@ccpo.odu.edu, enright@ccpo.odu.edu

ABSTRACT

Large-eddy simulation (LES) of Langmuir circulation in a wind-driven shear current in shallow water is reported. After the introduction and a brief description of the governing equations and the numerical method, we focus on the major differences in the dynamics between wind shear-driven Couette flow and the same flow with Langmuir circulation. This comparison will rely on flow visualizations and diagnostics including mean velocity profiles, invariants of the resolved Reynolds stress anisotropy tensor and balances of the transport equations for resolved mean turbulent kinetic energy and resolved Reynolds stress tensor.

INTRODUCTION

Langmuir circulation (LC), often occurring in the wind and wave driven surface mixed layer of lakes and oceans, consists of pairs of parallel counter-rotating vortices (or cells) oriented approximately in the streamwise direction. Originally characterized by Langmuir (1938), Langmuir cells are thought to be generated by interaction between the wind-driven mean shear current and the Stokes drift current caused by surface gravity waves.

Over the last several decades, numerous field observations of LC have been made using acoustic Doppler current profilers. Most of these works have recorded LC in the ocean surface mixed layer over deep water. Recent observations (Gargett et al., 2004 and Gargett and Wells, 2005) made on the shallow shelf off the southern coast of New Jersey in the presence of strong wind and wave forcing led to the discovery of LC extending throughout the entire water column. Such patterns reaching down to the bottom boundary layer have been termed *supercells* because of their profound influence on sediment resuspension and transport.

LES of LC performed up to date have also focused on the surface mixed layer over deep water, far from the bottom boundary layer. Recent simulations include those of Skyllingstad and Denbo (1995), McWilliams et al. (1997), and Li et al. (2004). Skyllingstad and Denbo found that wave forcing (creating LC) plays a bigger role than convective forcing in generating mixing. McWilliams et al. included the Coriolis force as well as LC forcing and found enhanced vertical turbulent velocity fluctuations due to LC. Li et al. performed a number of simulations and found differences in the turbulence structure between convection-dominated, shear-dominated and Langmuir-dominated turbulence.

We report LES of Langmuir supercells approximating the conditions observed by Gargett et al. (2004) and Gargett and Wells (2005: henceforth GW). To that extent, Couette flow was simulated with a stationary, no-slip plane at the bottom and a constant streamwise, tangential stress boundary condition at the top surface approximating the effect of a constant wind shear stress (see figure 1). The governing equations were augmented with the Craik-Leibovich (CL) force (Craik and Leibovich, 1976) accounting for LC.

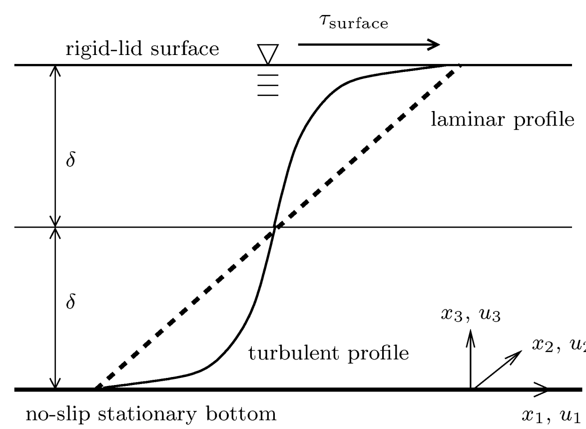

Figure 1: Sketch of Couette flow driven by surface stress, τ_{surface}, due to wind. The total depth is H and $\delta = H/2$. ——— , mean velocity profile in a turbulent flow; - - - - , linear velocity profile in a laminar flow.

Over the last decade, numerous direct numerical simulations of traditional turbulent plane Couette flow have been carried out. A common feature observed in these studies is the presence of streaks of high (positive) and low (negative) streamwise velocity fluctuations on horizontal (x_1-x_2) planes near the central or core region of the channel. These large-scale streaks possess much greater length scales than the classical *wall streaks* observed on near-wall horizontal planes of Poiseuille flow. When visualizing the flow on spanwise-vertical (x_2-x_3) planes the large-scale streaks appear as cell patterns extending nearly from top to bottom, similar to the Langmuir supercell patterns observed in shallow shelf seas. The spanwise length of the Couette cells and streaks is approximately equal to the channel height or depth (Lee and Kim, 1991). Lee and Kim showed that the presence of the Couette cells and streaks were not an artifact of the limited streamwise (x_1) and spanwise length (x_2). Through direct numerical simulation, Papavassiliou and Hanratty (1997) provided insight into the dynamics governing the cells and streaks. They found that the large-scale Couette cells can receive energy from the small-scale turbulence, contrary to the common energy cascade notion in which the large-scales always pass down energy to the small-scales.

After a brief description of the governing equations and numerical method, we focus on the major differences in the dynamics between wind shear-driven Couette flow and the same flow with LC under the conditions observed by GW.

GOVERNING EQUATIONS AND NUMERICAL METHOD

Constant density flow is assumed because the shallow water Langmuir supercells described by GW were observed in approximately neutrally stable water. The non-dimensionalized, filtered, incompressible Navier-Stokes equations augmented by the CL vortex force accounting for LC are

$$\begin{aligned}\frac{\partial \bar{\mathbf{u}}}{\partial t} + \nabla \cdot (\bar{\mathbf{u}} \otimes \bar{\mathbf{u}}) &= -\nabla \bar{p} + \frac{1}{\mathrm{Re}} \Delta \bar{\mathbf{u}} + \nabla \cdot \mathbf{T} \\ &\quad + \frac{1}{\mathrm{La}_{\mathrm{T}}^2} \bar{\mathbf{F}}_{\mathrm{CL}} \qquad (1) \\ \nabla \cdot \bar{\mathbf{u}} &= 0\end{aligned}$$

where an over-bar denotes a filtered quantity, $\bar{p}$ is the filtered modified pressure (McWilliams et al., 1997) divided by density ρ, and the filtered velocity is $\bar{\mathbf{u}} = (\bar{u}_1, \bar{u}_2, \bar{u}_3)$ in coordinate system $\mathbf{x} = (x_1, x_2, x_3)$ (figure 1).

The filtered vortex force on the right hand side is

$$\bar{\mathbf{F}}_{\mathrm{CL}} = \mathbf{u}_{\mathrm{s}} \times \bar{\omega} \qquad (2)$$

modeling the mechanism behind LC (Craik and Leibovich, 1976); *i.e.* the interaction between surface gravity wave Stokes drift velocity, $\mathbf{u}_{\mathrm{s}}$ and the shear flow represented by the filtered vorticity $\bar{\omega}$. The mechanism consists of tilting and stretching of vertical vorticity into the horizontal by the Stokes drift velocity, resulting in enhanced streamwise vorticity.

The equations are non-dimensionalized using the friction velocity $u_\tau = (\tau_{\mathrm{surface}}/\rho)^{1/2}$ and the channel mid-depth $\delta = H/2$, thus leading to a Reynolds number $\mathrm{Re}_\tau = u_\tau \delta/\nu$. The non-dimensionalization of the CL force, $\bar{\mathbf{F}}_{\mathrm{CL}}$, gives rise to the turbulent Langmuir number, $\mathrm{La}_{\mathrm{T}} = (u_\tau/u_{\mathrm{s}})^{1/2}$, appearing in (1). Note that $\mathrm{La}_{\mathrm{T}} = \infty$ corresponds to $u_{\mathrm{s}} = 0$, that is zero Stokes drift velocity and thus no LC. As $\mathrm{La}_{\mathrm{T}} \to 1$ LC becomes comparable to the shear flow, while for $\mathrm{La}_{\mathrm{T}} < 1$ LC dominates. The Stokes drift velocity appearing in (1) is

$$\mathbf{u}_{\mathrm{s}} = u_{\mathrm{s}} \left(\frac{\cosh[2k(x_3 - H)]}{2 \sinh^2(kH)} \right) \mathrm{e}_1 \qquad (3)$$

(Phillips, 1967) where e_1 is the unit vector in the x_1-direction. The coefficient u_{s}, also appearing in the definition of La_{T}, is defined as $u_{\mathrm{s}} = \sigma k a^2$, where σ is the dominant frequency, k is the dominant wavenumber and a is the amplitude of the surface gravity waves.

The *subgrid-scale (SGS) stress* in (1) is defined as

$$\mathbf{T} = \bar{\mathbf{u}} \otimes \bar{\mathbf{u}} - \overline{\mathbf{u} \otimes \mathbf{u}} \qquad (4)$$

where the term $\overline{\mathbf{u} \otimes \mathbf{u}}$ gives rise to a closure problem. The deviatoric part of $\mathbf{T}$ is parameterized and the dilatational part is added to $\bar{p}$. The following parameterization (Smagorinsky, 1963) is used:

$$\mathrm{dev}\{\mathbf{T}\} = 2\nu_{\mathrm{T}} \nabla^{\mathrm{s}} \bar{\mathbf{u}} \qquad (5)$$

where the eddy viscosity is given as

$$\nu_{\mathrm{T}} = (C_{\mathrm{s}} \bar{\Delta})^2 |\nabla^{\mathrm{s}} \bar{\mathbf{u}}| \qquad (6)$$

and

$$\begin{aligned}\nabla^{\mathrm{s}} \bar{\mathbf{u}} &= \frac{1}{2} \left\{ \nabla \bar{\mathbf{u}} + (\nabla \bar{\mathbf{u}})^{\mathrm{transpose}} \right\} \qquad (7) \\ |\nabla^{\mathrm{s}} \bar{\mathbf{u}}| &= (2\, \nabla^{\mathrm{s}} \bar{\mathbf{u}} \cdot \nabla^{\mathrm{s}} \bar{\mathbf{u}})^{1/2} \qquad (8)\end{aligned}$$

are the filtered strain rate tensor and its norm, respectively. The coefficient $(C_{\mathrm{s}} \bar{\Delta})^2$, is computed dynamically using the procedure described by Lilly (1992).

In our LES we use a free-slip, rigid-lid approximation for the water surface thus filtering out surface gravity waves. Zhou et al. (1998) performed simulations of LC with a surface wavy boundary layer due to a second order Stokes wave and compared results to a simulation with a free-slip, rigid-lid approximation including the CL vortex force. The simulations were in general agreement, demonstrating the validity of the free slip, rigid-lid model with CL vortex forcing.

The numerical method used employs a hybrid spectral/finite difference discretization. Horizontal directions (x_1 and x_2) are discretized spectrally via fast Fourier transforms and the vertical direction (x_3) is discretized via high order (fifth and sixth) compact finite difference schemes, allowing for grid stretching in the vertical in order to resolve expected strong vertical gradients in the velocity. Boundary conditions are no-slip velocity at the bottom wall and constant shear stress and zero normal flow ($\bar{u}_3 = 0$) at the top rigid-lid surface. Periodicity is assumed in the horizontal directions. Time-marching consists of a second order time-accurate fractional step scheme.

NUMERICAL RESULTS

In this section, we compare the following two cases: 1) Couette flow driven by a surface wind stress with CL vortex forcing and 2) Couette flow driven by a surface wind stress without LC. In both cases, the constant surface wind stress is applied such that $\mathrm{Re}_\tau = 180$. Case 1) is characterized by $\mathrm{La}_{\mathrm{T}} = 0.7$ and $\lambda = 6H$. These values for La_{T} and λ are representative of the coastal shelf shear flow with Langmuir supercells observed by GW. Case 2) is characterized by $\mathrm{La}_{\mathrm{T}} = \infty$, thus no LC. Note that Re_τ representative of the observations is much greater than that of the present simulation ($\mathrm{Re}_\tau = 180$). Although not reported here, simulations with LC at higher Reynolds numbers were performed without great changes in the results, demonstrating that the simulation at $\mathrm{Re}_\tau = 180$ is not adversely affected by low Reynolds number effects.

Following the direct numerical simulations of traditional Couette flow at about $\mathrm{Re}_\tau = 170$ of Lee and Kim (1991), the domain dimensions for both cases, 1) and 2), were chosen as $(L_1/\delta, L_2/\delta, L_3/\delta) = (4\pi, 8\pi/3, 2)$. Here L_1, L_2 and L_3 are the lengths of the domain in the x_1-, x_2-, and x_3-direction, respectively. The computational grid for the Couette flow with no LC contained 33 points in x_1, 65 points in x_2 and 65 points in x_3 ($33 \times 65 \times 65$). A greater number of points in the x_3-direction was required for Couette flow with LC in order to resolve stronger vertical gradients, thus the grid had ($33 \times 65 \times 97$) points. The non-dimensionalized time step was chosen as 0.0025 and 0.005 for the cases with and without LC, respectively, in order to yield temporal accuracy and not violate the CFL condition.

Visualizations

Figure (2) shows contours of instantaneous streamwise fluctuating velocity, u_1', on the horizontal plane at the middle of the channel. In both cases of the Couette flow (with LC and without LC) there is at least one pair of high- and low-speed regions or streaks highly elongated in the streamwise direction (x_1) and alternating in the spanwise (x_2) direction. In the flow with no LC shown in figure (2b) the spanwise length of each region is approximately equal to the depth, H. Animations reveal that when the CL vortex force is turned on, the high-speed regions merge, as the flow transitions from two pairs of streaks to one pair. Figure (2a) shows the one-pair structure characterizing Couette flow with LC.

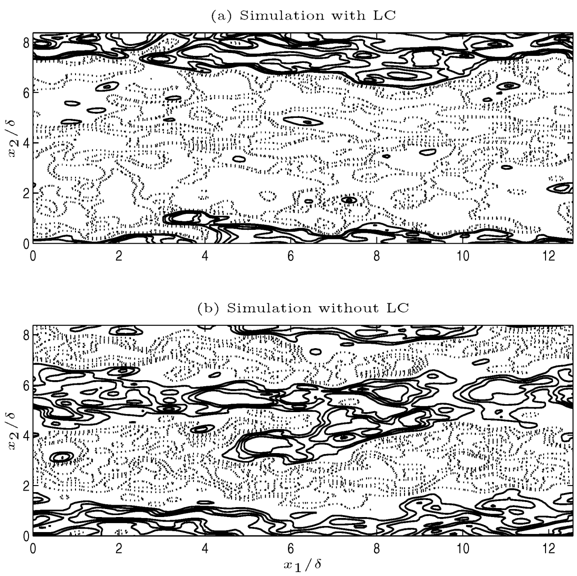

Figure 2: Instantaneous contours of u_1' on horizontal (x_1-x_2) plane at middle of channel ($x_3 = H/2$) in Couette flow with and without LC. Fluctuations u_1' are normalized by the mean centerline streamwise velocity, U_c. ········ , $u_1'/U_c > 0$; ——— , $u_1'/U_c < 0$.

Figures (3) and (4) show the mean vertical structure of the fluctuating velocity components in the flow with and without LC, respectively. Overall, both flows exhibit positive and negative spanwise cell structures in each of the fluctuating velocity components; the flow with LC has a spanwise *one-cell* structure while the flow without LC has a spanwise *two-cell* structure. Furthermore, in the mean, flow with LC has much stronger maxima and minima in all fluctuating velocity components: extrema of $\ll u_1' >_t >_{x_1}$, $\ll u_3' >_t >_{x_1}$ and $\ll u_2' >_t >_{x_1}$ are approximately 3, 2.5 and 10 times greater, respectively.

As seen in figure (3a), the flow with LC is characterized by intensification of positive $\ll u_1' >_t >_{x_1}$ near the surface and near the bottom, in close agreement with the observations of GW. In the case of the flow without LC, there is no such intensification as the magnitude of $\ll u_1' >_t >_{x_1}$ is roughly uniform (either positive or negative) in most of the water column. Note that in the observations, quantities are averaged over time only and not over time and streamwise direction or over time and horizontal directions, as is done here.

In both flows, a region of positive $\ll u_1' >_t >_{x_1}$ coincides with a region of negative $\ll u_3' >_t >_{x_1}$ and vice-versa. Regions of positive $\ll u_3' >_t >_{x_1}$ are referred to as *upwelling limbs* and regions of negative $\ll u_3' >_t >_{x_1}$ are referred to as *downwelling limbs*. At mid-depth in the flow with LC, the ratio of spanwise length of the upwelling limb to spanwise length of the downwelling limb is 1.6, in close agreement with the observational value of 1.5. In the flow without LC this ratio is approximately 1. Additionally, the downwelling limbs in the observations and in the the flow with LC possess greater intensity (magnitude) of $\ll u_3' >_t >_{x_1}$ than their adjacent upwelling limbs. In the the flow without LC, the magnitude of $\ll u_3' >_t >_{x_1}$ in the downwelling limbs is nearly the same as in the upwelling limbs.

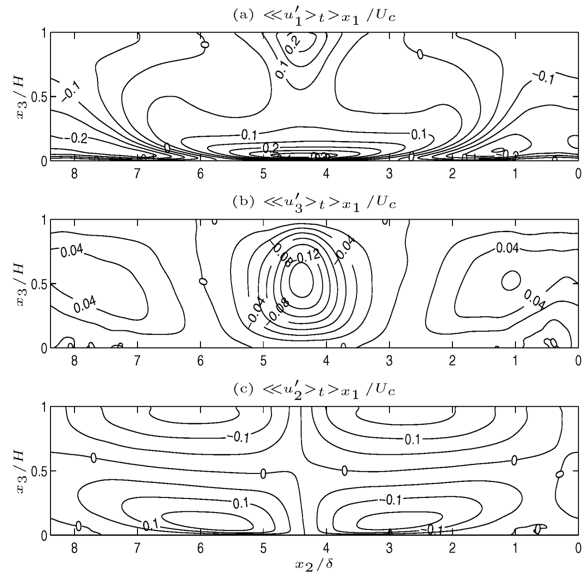

Figure 3: Contours of averaged fluctuating velocity components (normalized by U_c) on x_2-x_3 plane for Couette flow with LC. $\ll \cdot >_t >_{x_1}$ denotes averaging in time and over x_1. $< \cdot >$ corresponds to averaging in time and over x_1 and x_2.

Furthermore, as seen in figures (3c) and (4c), in both flows a region of upwelling coincides with a region where negative spanwise (x_2) gradient of $\ll u_2' >_t >_{x_1}$ occurs near the surface. The opposite trend is seen near the bottom; a region of upwelling coincides with a region where positive spanwise gradient of $\ll u_2' >_t >_{x_1}$ occurs near the bottom. Finally, in the flow with LC, extrema of $\ll u_2' >_t >_{x_1}$ occur at the surface (similar to the field observations), in contrast to the flow without LC where they occur in the upper third of the water column.

Color versions of the previous figures may be found in www.ccpo.odu.edu/∼tejada.

Mean Profiles, Resolved Reynolds Stresses and Invariants

Figures (5a) and (6a) show mean streamwise velocity for Couette flow with LC and without LC, respectively. In both cases the mean spanwise velocity $< u_2 >$ and the mean vertical velocity $< u_3 >$ (not shown) are nearly zero. A major difference between the two flows occurs in $< u_1 >$. In the flow with LC, the LC serves to homogenize $< u_1 >$ throughout most of the water column. This behavior can be seen in figure (6a) where $< u_1 >$ is roughly constant throughout most of the water column. In the flow without LC, $< u_1 >$ has non-zero slope throughout the water column.

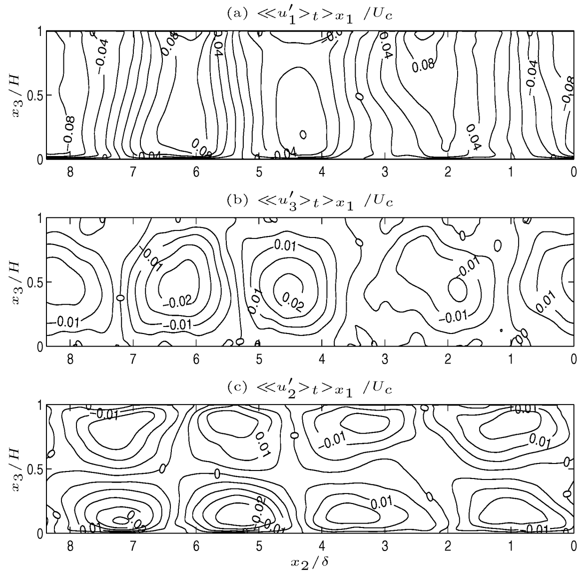

Figure 4: Contours of averaged fluctuating velocity components (normalized by U_c) on x_2-x_3 plane for Couette flow without LC.

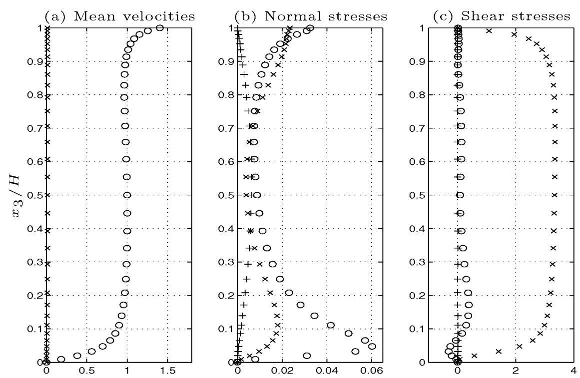

Figure 5: Profiles of mean velocity and resolved Reynolds stresses for Couette flow with LC. In (a): $\circ$, $<u_1>$; $\times$, $<u_2>$. In (b): $\circ$, $<u_1'u_1'>$; $\times$, $<u_2'u_2'>$; $+$, $<u_3'u_3'>$. In (c): $\circ$, $-<u_1'u_2'>$; $\times$, $-<u_1'u_3'>$; $+$, $-<u_2'u_3'>$. Velocities and and stresses are normalized by U_c and U_c^2 respectively.

Figures (5b) and (6b) show resolved normal Reynolds stress components for Couette flow with and without LC, respectively. There are several distinguishing differences between the two cases. First, the LC case possesses larger values of $<u_2'u_2'>$ and $<u_3'u_3'>$ than the case without LC, especially in the lower part of the water column. In the no LC case, ordering of components is $<u_1'u_1'> \; > \; <u_2'u_2'> \; > \; <u_3'u_3'>$ for the entire water column. In the LC case, this ordering changes, as in the lower part of the water column $<u_1'u_1'> \; > \; <u_2'u_2'> \; > \; <u_3'u_3'>$ while in the middle $<u_1'u_1'> \; > \; <u_3'u_3'> \; > \; <u_2'u_2'>$. Towards the upper part of the water column the ordering changes to $<u_2'u_2'> \; > \; <u_1'u_1'> \; > \; <u_3'u_3'>$, and at the surface it settles back to $<u_1'u_1'> \; > \; <u_2'u_2'> \; > \; <u_3'u_3'>$. The normalized magnitudes of the resolved normal Reynolds stress components in the LC case are much closer to those recorded in the field observations of GW, especially in the lower part of the water column.

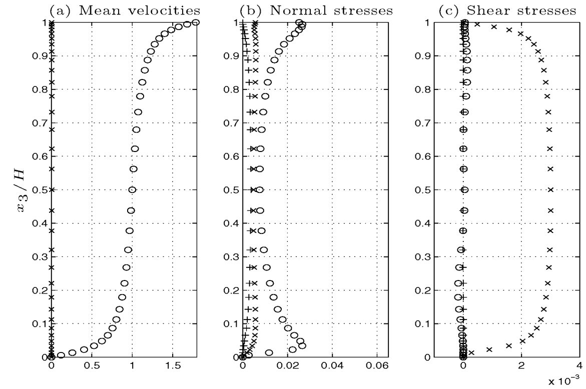

Figure 6: Profiles of mean velocity and resolved Reynolds stresses for Couette flow without LC. Symbols follow the same convention as in figure (5).

Figures (5c) and (6c) show resolved shear Reynolds stress components for the flow with and without LC, respectively. $<u_1'u_3'>$ components for both cases are close to each other in magnitude throughout most of the water column; for the LC case, $<u_1'u_3'>$ attains slightly greater values, especially near the middle of the water column. The normalized magnitude of $<u_1'u_3'>$ in both cases is in close agreement to that recorded in the field observations. Additionally, for both cases, $<u_2'u_3'>$ is nearly zero throughout the entire water column, similar to the observations. For Couette flow without LC, this also occurs with $<u_1'u_2'>$. In Couette flow with LC, $<u_1'u_2'>$ is nearly zero throughout most of the water column, except for the bottom part where the CL vortex force induces slight variations. Of importance is the fact that the data recorded in the field observations exhibit a $<u_1'u_2'>$ component which is far from zero, perhaps due to a non-zero mean velocity in x_2, $<u_2>$ (see GW). This is in contrast to the current simulations for which $<u_2>$ is nearly zero.

Figures (7) and (8) show maps of the Lumley invariants ($\text{II} = b_{ij}b_{ji}$ and $\text{III} = b_{ij}b_{jk}b_{ki}$, (Pope, 2000)) for Couette flow with and without LC. The quantity $\text{II}^{1/2}$ serves as a measure of the magnitude of the anisotropy, while the location of the coordinate $(\text{II}^{1/2}, \text{III}^{1/3})$ serves as a measure of the *shape* of the anisotropy. Figures (7) and (8) show the trajectories of the Lumley invariant maps varying from $x_3/H = 0$ (bottom wall) to $x_3/H = 1$ (top surface). For both flows with and without LC, the fluctuating motion is two-component (near the top bounding curve of the Lumley *triangle*) very close to the bottom wall because $<u_3'u_3'>$ is much smaller than the other two normal Reynolds stress components. In the case of Couette flow without LC, the fluctuating motion moves close to a cigar-shaped axisymmetric state (near the right hand side edge of the triangle) as the distance away from the bottom wall increases. The reason for this behavior is that $<u_1'u_1'>$ is larger than $<u_2'u_2'> \approx <u_3'u_3'>$, especially in the middle region of the water column. In the upper-half region of the channel, the fluctuating motion moves back towards the two-component state.

In contrast, for the case with LC, as distance from the wall increases the turbulence moves towards a pancake-shape state as the trajectory of the map goes into the interior of the triangle towards the left hand side edge. The reason for this behavior is that $<u_1'u_1'>$ and $<u_2'u_2'>$ are much greater

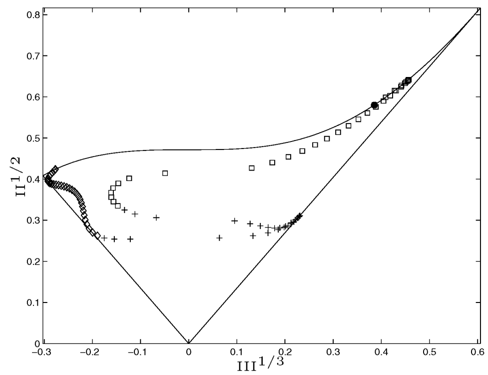

Figure 7: Lumley triangle for Couette flow with LC: □ , $0 < x_3/H \leq 1/3$; ○ , $1/3 < x_3/H \leq 2/3$; ◇ , $2/3 < x_3/H \leq 1$. The solid square denotes the map at the first point off the wall.

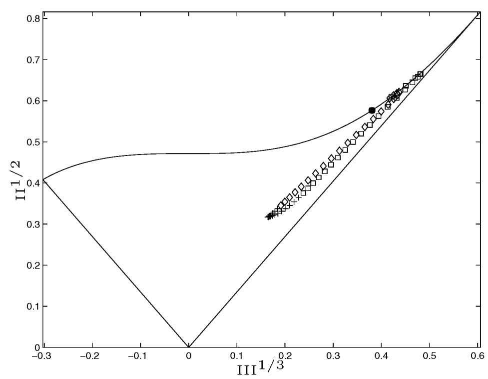

Figure 8: Lumley triangle for Couette flow without LC. Symbols follow the same convention as in figure (7).

than $<u_3'u_3'>$ throughout much of the bottom third portion of the water column. This is no longer true in the mid-depth region as the ordering $<u_1'u_1'> \; > \; <u_3'u_3'> \approx <u_2'u_2'>$ holds and the turbulence shifts back towards an axisymmetric cigar-shape state. In the upper-half of the channel, as distance towards the top surface decreases, the turbulence moves back towards the pancake-shape state. At the surface, the turbulence assumes an approximately two-component isotropic state (the upper left hand side vertex of the triangle) because $<u_1'u_1'> \approx <u_2'u_2'>$ and $<u_3'u_3'> = 0$. Of great importance is that the *c-shaped* trajectory of the Lumley invariant map for Couette flow with LC (figure (7)) closely resembles the shape of the map based on data from the field observations of GW. Furthermore, it highlights the vast difference in turbulent motion between Couette flow with and without LC.

Budgets

Figure (9) contrasts the budget terms for transport of mean resolved turbulent kinetic energy (TKE) in both flows close to the bottom wall. The main difference here is the presence of the CL vortex force (denoted by plus symbols in figure (9a)) acting as a sink in the flow with LC. This sink is partially balanced by pressure transport (denoted by the dashed line). In the flow without LC (figure (9b)), the CL vortex force is zero and thus the pressure transport is practically dormant. At the wall, in both cases, viscous diffusion (denoted by dots) serves to balance viscous dissipation (denoted by squares).

Near the top surface, the transport of mean TKE follows different dynamics in the two cases, as depicted by figure (10). In flow with LC, the CL vortex force acts as a source of TKE, reaching a maximum at the top surface and is mostly balanced by a negative pressure transport. In the case with no LC, the pressure transport is nearly zero given that the CL force is zero. The rest of the terms in the two cases only show slight differences.

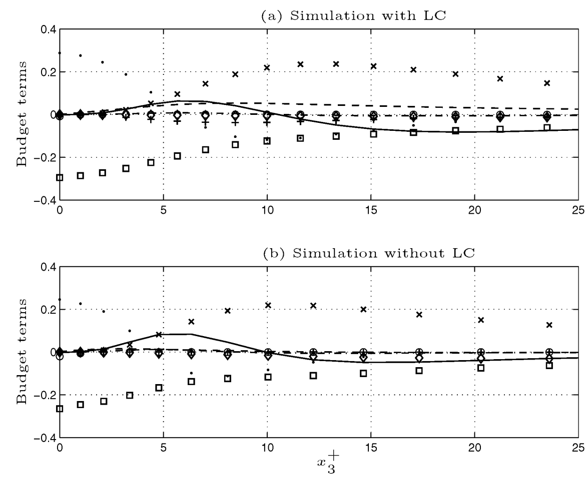

Figure 9: Near bottom wall budget terms in transport equation for turbulent kinetic energy. Terms are normalized by viscous scales (Pope, 2000); location of wall is at $x_3^+ = 0$. ——— , turbulent transport; – – – – , pressure transport; – · – , SGS transport; • • • , viscous diffusion; □ , viscous dissipation; ◇ , SGS dissipation; × , production by shear; + , production by CL force (Langmuir); ○ , sum of all terms.

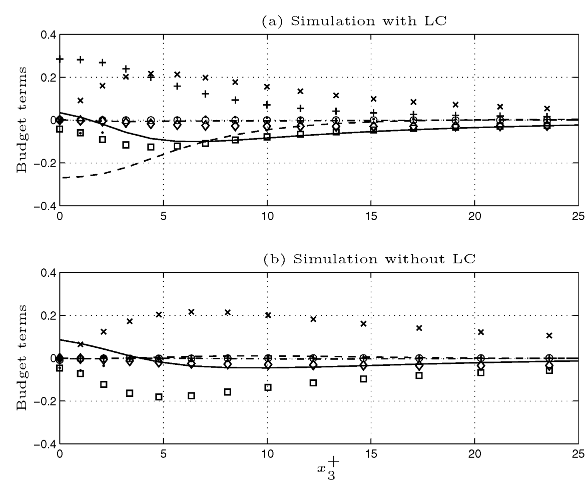

Figure 10: Near top surface budget terms in transport equation for resolved turbulent kinetic energy. Terms are normalized by viscous scales; location of top surface is at $x_3^+ = 0$. Symbols follow same convention as in figure (9).

Figures (11) and (12) contrast the budget terms for transport of $- <u_1'u_3'>$ (the dominant component of the shear Reynolds stress) in Couette flow with and without LC. In the case with LC, near the wall (figure (11a)) pressure transport serves to balance CL vortex forcing and pressure-strain redistribution (denoted by stars). At the wall, in the case with no LC (figure (11b)) pressure transport balances pressure-strain redistribution, as the CL vortex force is zero. For the region $x_3^+ > 5$ appearing in the figure, production by shear (denoted by the x-marks) plays a bigger role than pressure transport as they both serve to balance pressure-strain redistribution. In the simulation with LC, production by shear is negligible as most of the source is provided by turbulent transport.

It is remarkable that the near-wall dominant terms in the flow without LC (i.e. pressure transport and pressure-strain redistribution) are an order of magnitude smaller than the near-wall terms in the flow with LC. This same disparity is also noted between dominant terms near the top surface (figure (12). In the case with LC, the dominant terms are once again pressure transport, the CL vortex force, and pressure-strain redistribution. Meanwhile in the case without LC, the dominant terms are production by shear, pressure transport, turbulent transport, and pressure-strain redistribution.

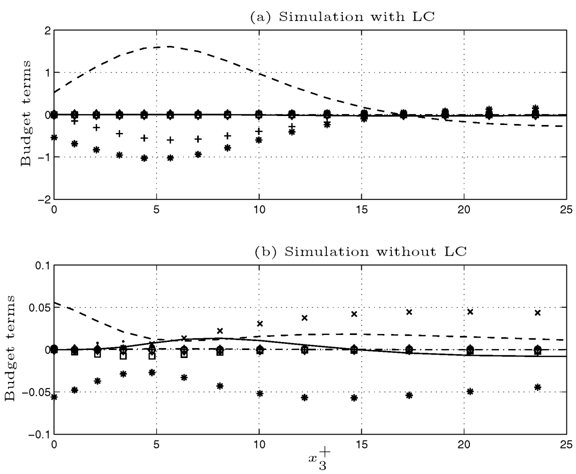

Figure 11: Near bottom wall budget terms in transport equation for $-<u_1'u_3'>$. Terms are normalized by viscous scales. *, pressure-strain redistribution; the rest of the symbols follow the same convention as in figure (9).

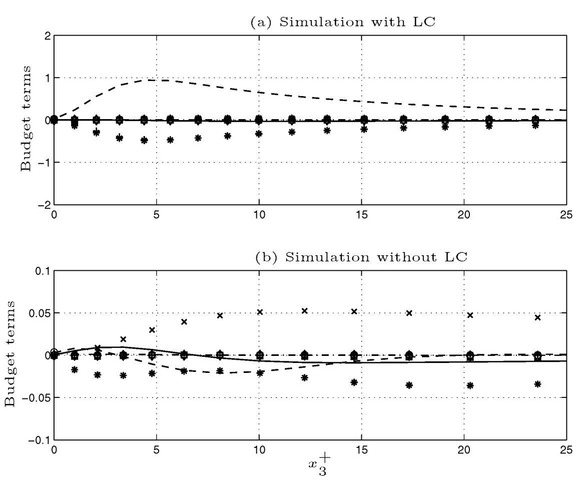

Figure 12: Near top surface budget terms in transport equation for $-<u_1'u_3'>$. Terms are normalized by viscous scales. Symbols follow the same convention as in figure (11).

CONCLUSIONS

Stress driven Couette flow with LC is very different from that without LC. The differences are present in all of the diagnostics shown. Also, the presence of LC results in greatly enhanced vertical mixing. Finally, basic features of the flow with LC are in general agreement with the field observations of GW.

ACKNOWLEDGEMENTS

This work was supported by the National Science Foundation under Grant OCE-0136403.

REFERENCES

Craik, A. D. D., and Leibovich, S., 1976, "A Rational Model for Langmuir Circulations", *Journal of Fluid Mechanics*, Vol. 73, pp. 401-426.

Gargett, A., Wells, J., Tejada-Martínez, A. E., and Grosch, C. E., 2004, "Langmuir Supercells: A Dominant Mechanism for Sediment Resuspension and Transport", *Science*, Vol. 306, pp. 1925-1928.

Gargett, A., and Wells, J., 2005, "Characteristics of Langmuir turbulence observed in shallow water", *Proceedings, Turbulence and Shear Flow Phenomena 4*, Williamsburg, Virginia, USA.

Kim, J., Moin, P., and Moser, R., 1987, "Turbulence statistics in fully developed channel flow at low Reynolds number", *Journal of Fluid Mechanics*, Vol. 177, pp. 133-166.

McWilliams, J. C., Sullivan, P. P., and Moeng, C.-H., 1997, "Langmuir Turbulence in the Ocean", *Journal of Fluid Mechanics*, Vol. 334, pp. 1-30.

Langmuir, I., 1938, "Surface Motion Induced by Wind", *Science*, Vol. 87, pp. 119-123.

Lee, M. J., and Kim, J., 1991, "The Structure of Turbulence in a Simulated Plane Couette Flow", *Proceedings, Eighth Symposium on Turbulent Shear Flows*, Munich, Germany, paper 5-3.

Li, M., Garrett, C., and Skyllingstad, E., 2005, "A Regime Diagram for Classifying Turbulent Large Eddies in the Upper Ocean", *Deep-Sea Research I*, Vol. 52, pp. 259-278.

Lilly, D. K., 1992, "A proposed modification of the Germano subgrid-scale closure", *Physics of Fluids*, Vol. 3, pp. 2746-2757.

Papavassiliou, D. V., Hanratty, T. J., 1997, "Interpretation of Large-scale Structures Observed in a Turbulent Plane Couette Flow", *International Journal of Heat and Fluid Flow.* Vol. 18, pp. 55-69.

Phillips, O. M., 1967, "Dynamics of the Upper Ocean", Cambridge University Press.

Pope, S. B., 2000, "Turbulent Flows", Cambridge University Press.

Skyllingstad, E. D., and Denbo, D. W., 1995, "An Ocean Large Eddy Simulation of Langmuir Circulations and Convection in the Surface Mixed Layer", *Journal of Geophysical Research*, Vol. 100, pp. 8501-8522.

Smagorinsky, J., 1963, "General circulation experiments with the primitive equations. I. The basic experiment", *Monthly Weather Review*, Vol. 91, pp. 99-164.

Zhou, H., Monismith, S., and Ferziger, J., 1998, "Numerical Simulation of Langmuir Circulation and its Comparison to Craik-Leibovich Theory", *Bulletin of the American Physical Society*, Vol. 43, pp. 2099-2099.